

An Advanced Hexacopter for Mars Exploration: Attitude Control and Autonomous Navigation


LAURA SOPEGNO 

University of Denver, Denver, CO 80210, USA
University of Palermo, Palermo, 90133, Italy


SIMONE MARTINI 

University of Denver, Denver, CO 80210, USA

SALVATORE PEDONE 

ADRIANO FAGIOLINI  Member, IEEE
University of Palermo, Palermo, 90133, Italy

MATTHEW J. RUTHERFORD  Member, IEEE

MARGARETA STEFANOVIC  Member, IEEE
University of Denver, Denver, CO 80210, USA

ALESSANDRO RIZZO  Senior Member, IEEE

Polytechnic of Turin, Turin, 10129, Italy

PATRIZIA LIVRERI  Senior Member, IEEE

University of Palermo, Palermo, 90133, Italy

KIMON P. VALAVANIS  Senior Member, IEEE

University of Denver, Denver, CO 80210, USA

Abstract—Mars exploration has recently witnessed major interest within the scientific community, particularly because unmanned aerial robotic platforms offer reliable alternatives for acquiring and collecting data and information from the Red Planet. However, the specific conditions of the Martian environment result in a restricted flight envelope when flying close to Mars and then landing on the surface of Mars. Therefore, in addition to the requirement to develop an aerial platform suitable for operations on Mars, autonomous navigation strategies and robust controllers are also needed for exploration tasks. It is argued that hexacopters with their relatively compact design represent a promising solution for autonomous exploration tasks on Mars, overcoming at the same time the limitations of wheel-based rovers. This research focuses on the design of a Mars Hexacopter (MHex) for a scouting mission in the Jezero region of Mars. The configuration and architecture of the hexacopter follow NASA conceptual study of the Mars Science Helicopter (MSH). Then, the mission profile for mapping Belva

Manuscript received XXXXX 00, 0000; revised XXXXX 00, 0000; accepted XXXXX 00, 0000.

Co-first authors: L. Sopegno, S. Martini. The authors contributed equally.

Corresponding authors: L. Sopegno, S. Martini, P. Livreri, Kimon P. Valavanis. Co-last authors: P. Livreri, K. P. Valavanis. The authors contributed equally.

email:laura.sopegno@du.edu simone.martini@du.edu
patrizia.livreri@unipa.it kimon.valavanis@du.edu

0018-9251 © 2022 IEEE

crater is examined, followed by a detailed approach to implement and test observer-based navigation and control strategies. A comprehensive simulated experiments environment based on the integration of ROS and Ardupilot, is also presented, used to validate the overall system architecture and mission parameters considering both the morphological shape of the explored crater and the atmospheric conditions of Mars.

Index Terms— Hexacopter, Mars, Nonlinear Control, Observer, Autonomous Navigation, SLAM.

I. Introduction

Unmanned missions for space exploration have emerged during the last two decades. Missions in Mars dominate the scientific interest as evidenced by the NASA Mars 2020 [1] project. In the most recent mission, the overall system included a robotic rover, Perseverance, and a small Mars Helicopter (MH), Ingenuity [2], [3] that were used to explore the Red Planet and look for signs of past life. The successful Ingenuity flights underlie the importance of UAVs when it comes to extraterrestrial exploration, and support the use of rotorcrafts in complex scenarios such as the Mars Sample Return (MSR) mission [4], [5], [6], where two helicopters may contribute to the transportation of terrain samples in collaboration with the rover's activity. Moreover, completion of such significant missions paves the way to future manned-unmanned exploration missions [7].

However, the current MH configuration has neither a specific scientific payload (P/L) nor enhanced onboard sensors, thus, limiting its capabilities to short flights over relatively flat and rock-free terrains [2]. Considering as a reference baseline the recent study of NASA Jet Propulsion Laboratory (JPL) and the Ames Research Center on the Mars Science Helicopter (MSH) [8], this research provides an in-depth analysis of an enhanced Mars Hexacopter (MHex) configuration, which includes shape and size of the main subsystems, as well as autonomous navigation and control strategies. The choice of a six-rotor rather than a quadrotor configuration is preferred because hexacopters demonstrate better stability, redundancy, payload capacity, and increased lifting power. Communication delays between the Earth and Mars cannot guarantee a continuously direct link for real-time data transfer, commands, and operations. For this reason, it is realistic to consider that: i.) the MHex will receive limited (transmitted - encoded) commands from the ground control station (GCS); ii.) the MHex will be able to autonomously navigate and execute specific tasks/missions in a GPS-denied environment; iii.) the MHex will maintain a stable attitude along its trajectory relying only on its onboard Guidance, Navigation and Control (GNC) system.

The objectives and aims of this research center around: i.) Providing an accurate model for the proposed MHex. Sizing, onboard sensors, tracking camera, 3D Lidar, and other equipment of the MHex are based on available data from [9], [10], [11]. ii.) Developing a simulator architecture for both the Martian environment and simulated

experiments by integrating ROS, Gazebo and Ardupilot, which allows for implementation and testing of SLAM, navigation, and control algorithms. iii.) Defining a specific mission profile for which SLAM and autonomous navigation strategies are developed. As such, implementation of the Unknown Input Observer (UIO) [12] is adopted to estimate the MHex states and unknown disturbances that act on the system [13], [14], [15], [16], [17], [18]. Note that due to the atmospheric conditions on Mars [19], [20], the MHex flight envelop challenge is tackled by implementing model-based controllers for better trajectory tracking accuracy when compared to the default Ardupilot PID controller [21].

The rest of the paper is organized as follows: Section II defines the mission requirements according to the Mars atmospheric conditions, as well as the design and size of the MHex. Section III presents the onboard GNC system and the overall architecture of the simulator tool. Obtained results are given in Section IV. Section V concludes the paper.

II. Mission Profile and System Design

This section describes the mission profile of the MHex under the Martian atmospheric conditions in the Jezero region, where the Belva crater is located, together with the architecture of the hexacopter system.

A. Mars Atmosphere

The Martian atmosphere limits flight conditions and, in turn, the configuration of aerial vehicles. Because of such atmospheric conditions and composition, oxidizing power sources cannot be used, and the gravitational acceleration g and atmospheric density ρ become the driving factors in lift generation. The low-density that reflects low Reynolds numbers, Re , in the range between 10000 to 25000, impacts significantly the airfoil design and aerodynamic performance, and suggests the use of lightweight materials for the hexacopter structure. Furthermore, the lower sound speed limits the rotors' maximum rotational speed. Table I compares the Earth and Mars atmosphere, also considering the atmospheric conditions of the Jezero region, which impact the design and analysis of the MHex. The sound speed on Mars refers to a Mach number (M) of 0.7.

TABLE I: Atmosphere comparison on Earth and Mars (Jezero region)

| | Unit | Earth | Mars |
|-------------------------|----------|-----------------------|-----------------------|
| Grav. acceleration, g | m/s^2 | 9.81 | 3.71 |
| Temperature, T | K | 288 | 223 |
| Density, ρ | kg/m^3 | 1.225 | 0.015 |
| Viscosity, μ | Ns/m^2 | 1.75×10^{-5} | 1.13×10^{-5} |
| Sound speed, a | m/s | 340.3 | 233.1 |
| Tip speed, V_{tip} | m/s | 238 | 163 |

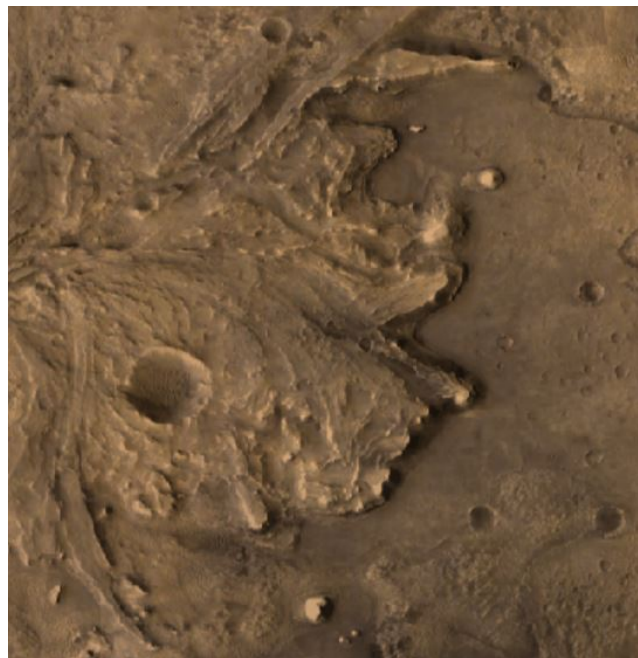


Fig. 1: Study area of the Belva crater in the Jezero region. Image obtained from the HiRISE dataset

B. Mission Requirements

The planned mission focuses on autonomous exploration of the Belva crater. A SLAM technique is adopted to collect data from the implemented autonomous mapping process (see Section IV). The MHex, as designed, increases the range of the examined terrain compared to traditional rovers [22], the endurance and range of which is limited because of ground obstacles and harsh terrains, such as craters and caves. Moreover, because of the near-surface flight altitude, the MHex guarantees a higher resolution than orbiters, resulting in a promising solution to better explore the Mars surface. For the mission under consideration, a 34 Km^2 area within and around the Belva crater is chosen for autonomous navigation and mapping, see Figure 1. This area is of scientific interest [23] as this region is related to the Mars 2020 Landing site [1] and it is deemed suitable for surficial deposits of ichnofossils as morphological evidence of past biological behavior. The whole mission consists of five segments: take-off, climb at the required altitude, cruise, descent and land (Figure 2). The flight trajectory is based on geological waypoints sent by the ground station to the MHex. After landing and recharging for 1 sol with solar panels, the MHex is expected to continue mapping with a target scanning range of about 3 Km^2 for each flight. This represents the operative area including slight deviations from a direct course. After mapping a consistent region, the MHex returns to the lander to download the collected scientific data to optimize the onboard processor weight and power management. A summary of the main mission parameters for the MHex is reported in Table II.

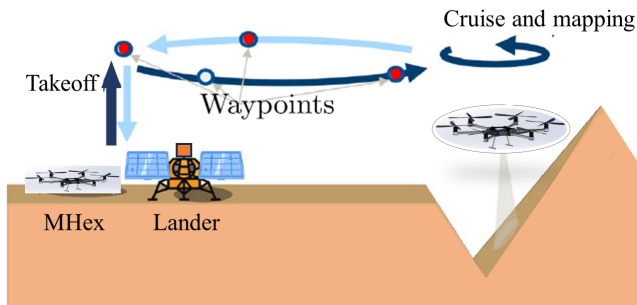


Fig. 2: MHex mission case for autonomous mapping of the Belva crater. Re-adapted from [24].

| | |
|-------------------|-------------------|
| P/L | 2.0 kg |
| Total flight area | 3 Km ² |
| Cruise speed | up to 8 m/s |
| Cruise altitude | 10 m |

TABLE II: Mission parameters for MHex-based autonomous mapping

C. System Architecture

Several studies using aerial vehicles for planetary exploration have already been conducted; a summary of the proposed configurations may be found in [25], [26]. However, findings in [27] show that a tailsitter design, which is a challenging system, have not offered any major advantage over a more conventional rotorcraft [28]. But as mentioned in Section I, the hexacopter configuration is a promising and robust design choice in this regard.

1. Mars Hexacopter sizing

The MHex design process starts with the definition of the mission requirements, thus the P/L identification. The MHex design is implemented in Solidworks, and the system sizing is based on the diameter of the rotor blade which is optimized for the required thrust in the Martian atmosphere. The six motors are sized with a 150% control margin for hover power, accommodating a motor speed up to 3008 rpm. The MHex blade is derived from the fluidic analysis in [8], considering the same diamond-shaped airfoils for the blade inboard sections with an 8% thickness-to-chord ratio and flight (hover and cruise) performance for M 0.55 to 0.8. The reference airfoil sections are already optimized for better stall behavior and lower power during flight. To account for modeling uncertainties, the MHex design includes a contingency weight factor equal to 20%, being the overall design at an early stage. Table III summarized the MHex parameters and weights, while Figure 3 shows the blade profile and the MHex architecture. The P/L is intended as a sensing payload, containing the 3D Lidar sensor for mapping the environment.

With respect to the MSH baseline [8], the whole airframe is increased (3m to 3.15m) to better compensate for drag effects acting on the rotors when rotating.

TABLE III: MHex design. Geometry and weights

| Parameters | Value | Unit |
|----------------------------|-------------|-----------|
| Airframe | 15.5 | Kg |
| Structure | 5.9 | Kg |
| Propulsion | 4.3 | Kg |
| Avionics and equipment | 2.7 | Kg |
| Contingency (20%) | 2.58 | – |
| P/L | 2.0 | Kg |
| Gross weight | 17.5 | Kg |
| Disk radius | 0.64 | m |
| Rotor numbers | 6 | – |
| Blades per rotor | 4 | – |
| Rotor average speed range | 2483 | rpm |
| length | 3.15 | m |
| Airframe size width | 3.15 | m |
| height | 0.50 | m |

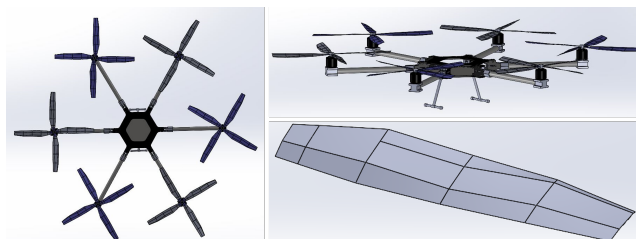


Fig. 3: Solidworks design of MHex structure and blade profile, 0.64 m disk radius, derived from airfoil sections in [8]

2. Sensors

The VLP-16 3D Lidar [29] is chosen as the primary sensor to perform the mapping of the Belva crater. Even though cameras represent a good solution in SLAM systems, the use of Lidars has enabled advances in the knowledge of planets such as the Moon, Mercury, Mars and several asteroids [30] representing a prominent technique in the future of planetary science. In 2019, a study on the geological investigation at the Lofthellir site (Iceland) was presented at the 50th Lunar and Planetary Science Conference [31] to address the potential exploration of lava tubes on the Moon and Mars through a 3D Lidar-equipped drone, showing preliminary good results and a successful mapping of the cave. Furthermore, recent studies performed by NASA aim to develop advanced precision landing technologies and accurate 3D scanning of the terrain through Lidar-based navigation [32] to optimize the descent and landing phase of landers. 3D Lidars can provide structural and rich information about the scanned environment, operating efficiently in low-light/varying illumination conditions. The generated point cloud provides depth information without the need for stereo matching or depth inference by directly capturing the geometry of the environment, reducing the need for complex feature extraction algorithms required by camera-based systems. The MHex Lidar tilting mechanism considers the exploration of both wide areas, such as craters, and caves, allowing obstacle detection and collision avoidance by scanning the surrounding ground

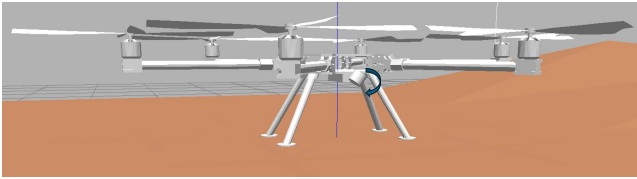


Fig. 4: MHex Lidar tilting mechanism, Gazebo simulation

and the vertical range with a rotation of 1 Hz (Figure 4). However, since a single-sensor SLAM system is usually fragile and full of uncertainty when performing localization, the MHex carries onboard three different sensors to perform precise SLAM navigation, as further described in Section III. Table IV provides a summary of the sensor features [33], [34] used onboard the MHex. The Garmin

TABLE IV: MHex Sensor Specifications

| Sensor | Frequency | Power | Range | Weight |
|-------------------------|-----------|-------|--------|--------|
| VLP-16 3D Lidar | 5-20 Hz | 8 W | <100 m | 590 g |
| t265 Tracking camera | 30-200 Hz | 1,5 W | 173° | 55 g |
| Lite v3 Altimeter | 10-30 Hz | 1,3 W | <40 m | 22 g |

Lite v3 altimeter, currently used onboard the Ingenuity helicopter [35], is a light, optical distance measurement sensor that uses infrared pulses of light projected down to the ground to measure the flight altitude of the MHex with respect to the ground.

D. Simulator: High-level Architecture

The Simulation environment relies on the integration of Ardupilot, a widespread open-source autopilot system, along with the Gazebo simulator and the Robot Operating System (ROS). This combination of free and open-source tools allows for simulating the dynamic behavior of the MHex model in a Mars-like environment, accounting for high accuracy of the numerous MHex attributes such as mass, inertia, wind gusts and noise thus allowing it to behave realistically when simulating. Because of the complexity of the simulated mission, extensive design and some software modification are required to achieve a realistic simulation. Particularly, continuous efforts in implementing advanced control strategies and integrating control techniques into the Ardupilot system not only highlight the significant adaptability of the software, but also allow researchers to develop in-depth analysis and get realistic results in complex simulation environments. Recent works considering the implementation of control strategies, such as the adaptive integral sliding mode control (AISMC) as well as the adaptive control integration into the Ardupilot software can be found in [36], [37]. Experiments on the adaptive method for the Ardupilot-based controller can also be found in [38] for fixed-wing

UAVs. For this research, the simulator runs on Ubuntu 20.04, with ROS Noetic, Gazebo 11.11.0, and Ardupilot Copter 4.3. Figure 5 displays an overview of the resulting workflow that the simulation environment allows.

E. Mathematical Modeling

To design model based controllers and considering the hexacopter configuration of Figure 6 the total thrust T and torques $\tau = [\tau_\phi \tau_\theta \tau_\psi]$ can be modelled as

$$\begin{bmatrix} T \\ \tau_\phi \\ \tau_\theta \\ \tau_\psi \end{bmatrix} = \begin{bmatrix} k & k & k & k & k & k \\ -k & k & \frac{\sqrt{3}k}{2} & -\frac{\sqrt{3}k}{2} & -\frac{\sqrt{3}k}{2} & \frac{\sqrt{3}k}{2} \\ 0 & 0 & -0.5k & 0.5k & -0.5k & 0.5k \\ b & -b & b & -b & -b & b \end{bmatrix} \begin{bmatrix} \Omega_1^2 \\ \Omega_2^2 \\ \Omega_3^2 \\ \Omega_4^2 \\ \Omega_5^2 \\ \Omega_6^2 \end{bmatrix} \quad (1)$$

where Ω_i is the i -th rotor's angular velocity while $k = 1.83 \times 10^{-4}$ and $b = 2.41 \times 10^{-5}$ are the thrust and drag coefficients of the propeller, respectively. These parameters are computed from hovering simulation as a result of the *LiftDrag* plugin aerodynamic effect. The complete mathematical model of the hexacopter can be obtained by considering the forces and torques of (1) into the general multirotor dynamical model

$$\ddot{p} = \frac{1}{m} T R e_3 - g e_3, \quad (2)$$

$$\ddot{\eta} = J_R^{-1} (\tau - C \dot{\eta}), \quad (3)$$

where p is the inertial position vector, m is the multirotor total mass, R is the rotation matrix from the body reference frame to the inertial reference frame which depends on the choice of Euler angles sequence $\eta = [\phi, \theta, \psi]^T$, $e_3 = [0, 0, 1]^T$ is the inertial z -axis vector, g the gravitational acceleration, $J_R = W^T J W$ the rotated inertia matrix with W being the matrix which relate angular velocities ω to Euler rates $\dot{\eta}$ and J the symmetric constant inertia matrix. C is the matrix accounting for centrifugal and Coriolis effects. The full description of the multirotor model can be found in [39].

F. Mars Hexacopter Model with ROS and Gazebo

The MHex model is exported from Solidworks to *urdf* file format, which is then converted to Gazebo's *sdf* format maintaining all inertial characteristic and meshes. The aerodynamic profile of the propellers is implemented using the *LiftDrag Plugin*, and the motor actuation from Ardupilot flight controller is managed through the *Ardupilot Gazebo Plugin*. To simulate the sensor fusion output, the odometry information is taken from an *odometry sensor* publishing up to 200 Hz. Indeed, given the Martian conditions, the Global Navigation Satellite System (GNSS), barometer, and magnetometer would not be available. To this end, these sensors are disabled and the alternative selection of sensors from Table IV, along with the IMU, is implemented to guarantee navigation, control, and mapping functionalities. Considering the use of a

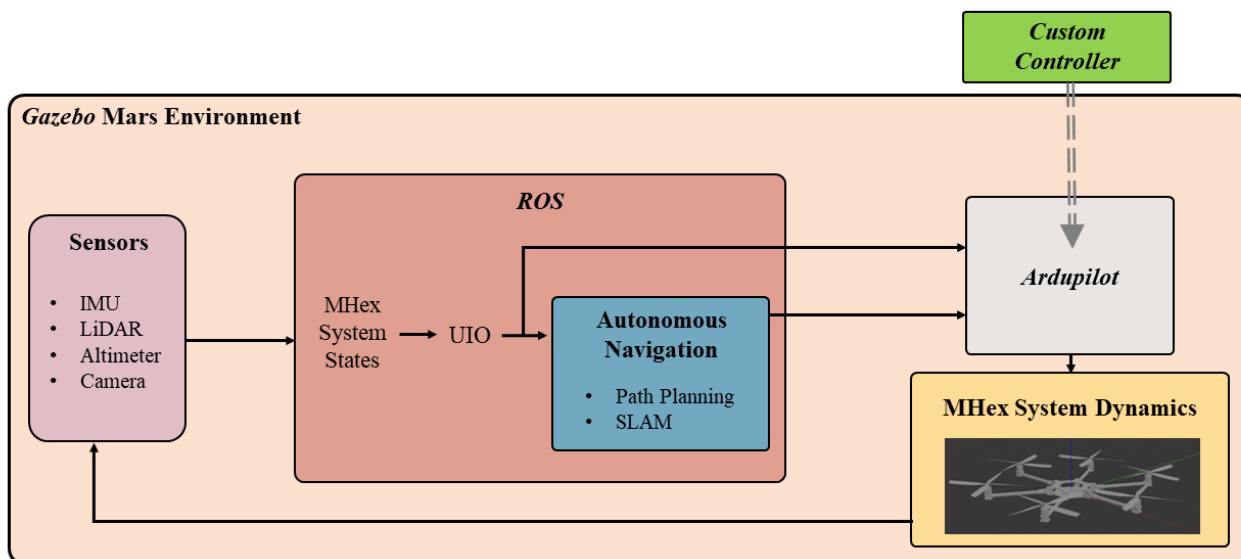


Fig. 5: Simulator Architecture

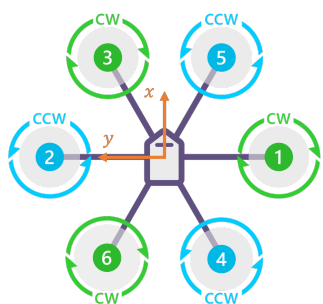


Fig. 6: Ardupilot Hexacopter X Configuration. Readapted from [40]

rotating VLP-16 Lidar, the spinning sensor is modeled and attached to the MHex body to account for its additional dynamics.

III. GNC System

As previously described, the MHex can explore harsh environments and remote areas otherwise denied to ground vehicles. For this reason, it requires a robust guidance, navigation and control (GNC) system to perform precise, GPS-denied autonomous navigation and advanced control stability. Moreover, in complex scenarios such as the Martian terrain, both stability and overall performance must go along with the robustness of the MHex against external and unknown disturbances acting on the system. A well-known category of filters developed in the last decades to address such issues refers to Kalman

filters. Particularly, a wide range of applications includes the Extended Kalman Filter (EKF) thanks to its simplicity and versatility in many operative contexts. Kalman filters provide an optimal estimation bounded under the strong assumption of Gaussian noise distribution, such as a complex tuning of parameters and covariance matrices, especially with high-dimensional systems.

The *Unknown Input Observer (UIO)* is an estimator that combines an easier design and robustness to modeling uncertainties in the system dynamics when compared to different types of filters and observers [41]. Indeed, as further shown in Section A.1, the UIO performances are higher than for the corresponding EKF, as it efficiently handles unknown external disturbances (e.g. wind gusts) together with good management of sensors' noise, guaranteeing the asymptotic convergence of the estimation error without prior assumptions of noise distribution or bounded unknown input signals, thus overcoming the limitations of the Kalman filters. Figure 7 provides the GNC framework for the MHex. In the proposed system, the *Perception and Estimation* block collects the measurements coming from a 3D Lidar, a downward laser altimeter, a tracking camera and the onboard IMU to obtain partial information about the MHex's state through the sensor fusion of different odometry estimations (Lidar Inertial Odometry, *LIO*, and Visual Inertial Odometry, *VIO*). Then, the UIO estimates both the unknown inputs of the dynamic system, which are not directly measured by the onboard sensors, and the full state of the MHex. The *Planning* block performs the optimal trajectory given a series of waypoints sent from the ground station, and the SLAM algorithm allows for

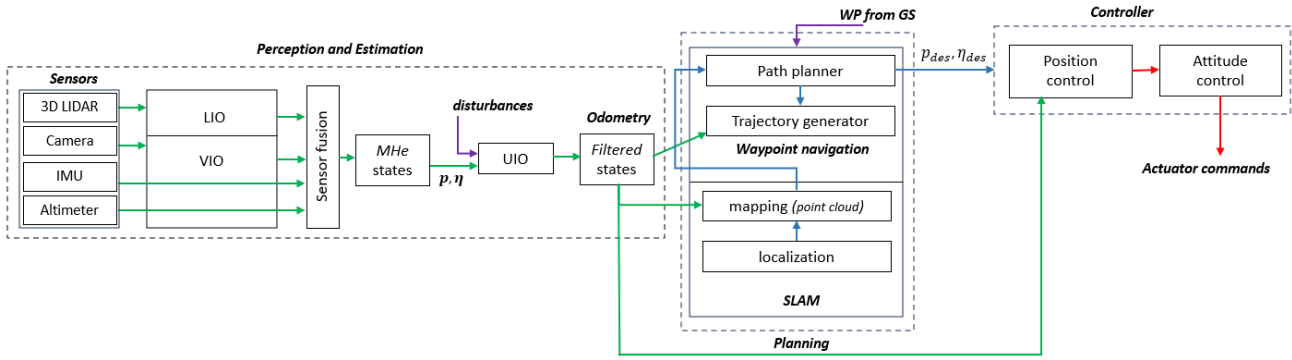


Fig. 7: GNC subsystem: Perception and Estimation, Planning and Control frameworks

the autonomous mapping of the surrounding environment, in turn sending feedback to the path planner for trajectory optimization. The *Controller* block computes the control action required to steer the MHex along the desired trajectory. Given the underactuated property of multirotors, the control structure is divided in outer (*position*) and inner (*attitude*) loop. The stock position controller within Ardupilot computes the attitude trajectory to reach the mission waypoints while the custom deployed inner loop controller provides the control action for attitude tracking. The following paragraph provides an in-depth analysis of the first two blocks, while the control strategies are discussed in paragraph B.

A. Autonomous Navigation Strategy

1. Unknown Input Observer Design

Single-sensor SLAM systems are usually fragile and full of uncertainty when performing localization. Considering the complexity of the mission when performing autonomous navigation, the MHex carries onboard three different sensors to perform precise SLAM, as shown in Figure 7. Multi-sensor fusion approach merges incoming information from the three sensors into a single, consistent estimate of the full MHex state by separately processing measurement data of each sensor and fusing them to achieve the latest state estimation. In the proposed scheme, *LIO* uses point cloud data to obtain both the MHex pose estimation and the 3D map of the environment, while *VIO* is in charge of achieving the pose estimation by combining visual sensor data and IMU data. The fusion of these two pieces of information, together with laser altimeter data for a more accurate altitude state, allows for an accurate estimation of the MHex state.

After obtaining preliminary information on the system with the onboard sensors, the UIO handles disturbances acting on the MHex and not directly measurable, such as external wind disturbances as well as sensor bias, and estimates the final MHex's states to be used for navigation and control. In the design of the UIO [42], [43], the state estimation process is decoupled from the unknown inputs, the latter reconstructed once the state estimation convergence is obtained. Following the reasoning in [12],

the linearized MHex system can be modeled in matrix form as:

$$\begin{aligned} \dot{x} &= Ax + Bu + W\delta \\ y &= Cx + Du + H\delta \end{aligned} \quad (4)$$

where $x \in \mathbb{R}^n$ is the state vector, $u \in \mathbb{R}^p$ and $\delta \in \mathbb{R}^v$ are the known and unknown input vectors respectively, $y \in \mathbb{R}^c$ is the output vector, and A, B, C, D, W and H are matrices of suitable dimensions. Without loss of generality, matrices D and H in (4) are assumed null, thus the output matrix only depends on the state. Considering the L -th Taylor series vectors U^L and Γ^L of the known and unknown inputs, i.e. $u(t)$ and $\delta(t)$, the L -th system's response vector is given by

$$Y^L = CA^L x + \sum_{i=0}^{L-1} CA^{L-1-i} (Bu^{(i)} + W\delta^{(i)}) \quad (5)$$

then, in the compact form

$$Y^L = O^L x + J_u^L U^L + J_\gamma^L \Gamma^L \quad (6)$$

where O^L is the L -th order observability matrix, while J_u^L and J_γ^L are the L -th order invertibility matrices corresponding to the known and unknown input signals. In this setting, following the analytical reasoning described in [43], an *Unknown Input Observer* for the system in (4) is given by

$$\dot{\hat{x}} = E\hat{x} + F(Y^L - J_u^L U^L) + Bu \quad (7)$$

with E and F two design matrices. Considering (6), a direct computation of the state estimation error dynamics, i.e. $\tilde{x} = \hat{x} - x(t)$, leads to

$$\begin{aligned} \dot{\tilde{x}} &= E\hat{x} + F(Y^L - J_u^L U^L) + Bu - Ax - Bu - W\delta = \\ &= E\tilde{x} + F(Y^L - J_u^L U^L) + (E - A)x - W\delta = \\ &= E\tilde{x} + FO^L x + FJ_\gamma^L \Gamma^L + (E - A)x - W\delta = \\ &= E\tilde{x} + (FO^L + E - A)x + FJ_\gamma^L \Gamma^L - W\delta \end{aligned} \quad (8)$$

and it is proved that, if the following conditions are simultaneously satisfied

$$\begin{aligned} FJ_\gamma^L &= [W, 0_{n \times v}] \\ E &= A - FO^L \end{aligned} \quad (9)$$

the estimation error dynamics takes the form

$$\dot{\tilde{x}} = E\tilde{x} \quad (10)$$

Finally, by virtue of an appropriate choice of the matrix E , the system in (10) can be made convergent to zero. The solvability of the above conditions can be satisfied if and only if (4) is invertible and strong observable, i.e. for some $L \leq n$ must hold

$$\text{rank}(J_\gamma^L) = v + \text{rank}(J_\gamma^{L-1}), \quad (11)$$

$$n = \text{rank}([O^L, J_\gamma^L]) - \text{rank}(J_\gamma^L) \quad (12)$$

2. 3D Lidar Mapping and Odometry

As described in the GNC framework of Figure 7, the *Planning* block is in charge of implementing the SLAM process along with the path planning algorithm. 3D Lidars permit to capturing of fine details of wide environments without being affected by variable illumination conditions. The SLAM method is also preferred in the context of the mission because of the complexity of autonomous navigation in a GPS-denied environment, thus a dedicated localization and mapping technique is required from the MHex to perform the mission tasks. The SLAM framework implemented onboard the MHex is shown in Figure 8. The SLAM system receives data

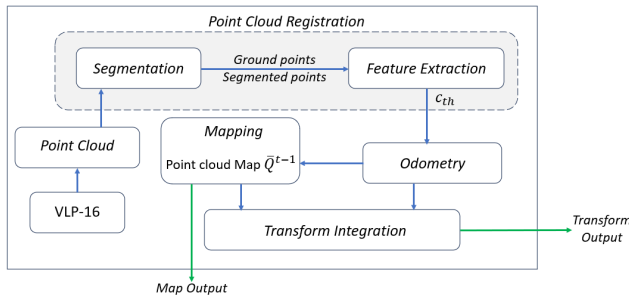


Fig. 8: 3D Lidar Odometry and Mapping system overview

input from the VLP-16 Lidar and then generates outputs regarding the computed map (*Map Output*) and the pose with respect to the generated map (*Transform Output*). The overall SLAM system is divided into four modules: In the *Point Cloud Registration* module, the *Segmentation* takes the scan's point cloud $P_t = \{p_1, p_2, \dots, p_n\}$ acquired at time t and, based on the VLP-16 horizontal and vertical resolution (0.2° and 2°) projects it onto a range image of resolution 1800 by 16. The points p_i in the point cloud are then represented in the range image by a unique pixel with a corresponding Euclidean distance r_i from the sensor. A second level of clustering is applied to the range image and the selected points are grouped into different clusters of 50 points each. A final selection only keeps and saves features of characteristic points (ground points and segmented points) in the range image allowing for an efficient computation of the entire data processing. In the *Feature Extraction* module the selected points are processed and sorted based on their roughness c with respect to a threshold c_{th}

$$c = \frac{1}{|S| \cdot |r_i|} \left\| \sum_{j \in S, j \neq i} (r_j - r_i) \right\| \quad (13)$$

with S the points set. Points for which $c > c_{th}$ are classified as *edge features*, while *planar features* for c smaller than c_{th} and then saved in two different sets F_e and F_p . In the *Odometry* module, the sensor motion is estimated between two consecutive scans by finding the corresponding features between points in the feature sets and the ones collected in the previous scan. The odometry algorithm performs at a high frequency (but low fidelity) to estimate the Lidar's velocity, while the *Mapping* algorithm runs at a lower frequency for fine matching of features in the set $\{F_e, F_p\}$ to a surrounding wider point cloud map Q^{t-1} and further registration of the point cloud. For a better computation of data, each feature set is stored in Q^{t-1} instead of a single point. Each feature set is associated with the pose of the Lidar when the scan is taken, considering the sensor FoV, and the selected feature sets are then transformed and fused into Q^{t-1} .

B. Controllers

This section briefly describes the control algorithms applied to the MHex. For the study case in analysis, the Ardupilot stock *PID* (*A-PID*) attitude controller [21] is compared through closed-loop simulations with custom deployed *PID* with feedback linearization (*PID-FL*) and *Backstepping* (*BC*) controllers.

1. PID-FL

PID is one of the most common controller in literature and industry due to its straightforward implementation and ease of tuning, including model based dynamic compensation into the loop has been shown to further improve tracking performance [39]. To this end, feedback linearization is used to exactly linearize the MHex non-linear dynamics. As such, the commanded torque vector is written as

$$\tau_c = J(\eta)v + C_\tau(\eta, \dot{\eta})\dot{\eta}, \quad (14)$$

so that the closed loop system becomes

$$\ddot{\eta} = v \quad (15)$$

which correspond to the following linear system

$$\dot{x} = Ax + Bv \quad (16)$$

where

$$A = \begin{bmatrix} 0_{3 \times 3} & I_{3 \times 3} \\ 0_{3 \times 3} & 0_{3 \times 3} \end{bmatrix}, B = \begin{bmatrix} 0_{3 \times 3} \\ I_{3 \times 3} \end{bmatrix}, x = \begin{bmatrix} \eta \\ \dot{\eta} \end{bmatrix} \quad (17)$$

hence, the virtual control vector v becomes the control action to be designed [44]. To show the performance improvement, the feedback linearization is placed in cascade to the Ardupilot attitude *PID* controller and, as such, the *A-PID* output value is assigned to v .

To be noted: the feedback linearization is performed using the nonlinear attitude model (3).

2. Backstepping

Backstepping (BC) model based control has been shown to be very effective in controlling nonlinear system in presence of noise and external disturbances [45]. The following BC controller is presented in [46], for brevity, only the commanded torque is listed here

$$\tau_{c,BC} = J(\ddot{\eta}_d - \Lambda^2 e) + C_\tau(\dot{\eta}_d + \Lambda e) + K_r r + K_i \int_0^t r dt \quad (18)$$

with orientation tracking error $e = \eta_d - \eta$, sliding mode error $r = \dot{e} + \Lambda e$, and Λ , K_r , K_i gain matrices to be tuned.

IV. Simulated Experiments

In the simulated mission scenario, the MHex performs the autonomous navigation along with SLAM given a series of waypoints sent from the ground control station. The takeoff is performed in the proximity of the crater region, having as the main focus the mapping of both the entire crater and surroundings. The MHex is required to perform collision-free flights during the mapping process, thus without prior information, and landing at the goal point when the last waypoint is reached. Table V gives the aerodynamic coefficients used to simulate the lift and drag experienced by the MHex during flight.

TABLE V: MHex aerodynamic parameters

| Parameters | α_0 | α_{st} | CL_α | CD_α | VLP-16 spin |
|------------|------------|---------------|-------------|-------------|-------------|
| Value | 0.0175 | 0.1920 | 7.791 | 0.55 | 1 Hz |

1. Observer Validation

As a first validation step, the comparison between the EKF and the UIO is implemented in Matlab/Simulink along a helix-based trajectory. For the EKF, the equivalent noise considered in the simulation follows a Gaussian distribution with $\mu = 0$ and variance $\sigma^2 = 0.01$, corresponding to the realistic sensor noise for both the t265 camera and the VLP lidar. Wind acting on the system is simulated along the horizontal and vertical directions. The modeling of the wind is also applied in the second validation step with ROS and Gazebo, as shown below. Then, the UIO is implemented along with the MHex system. To reach the form of (4), analytical calculations lead to the matrices

$$A = \begin{bmatrix} 0_{6 \times 6} & I_{6 \times 6} \\ 0_{6 \times 6} & 0_{6 \times 6} \end{bmatrix} \quad B = \begin{bmatrix} M & 0_{3 \times 3} \\ 0_{3 \times 3} & J \end{bmatrix} \quad (19)$$

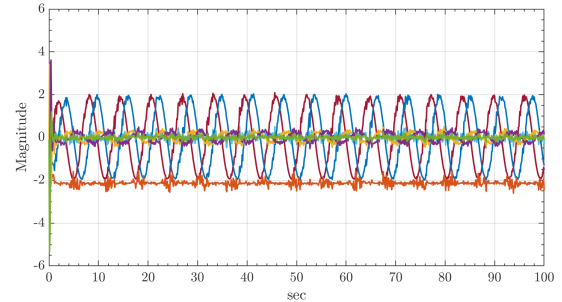
$$C = \begin{bmatrix} I_{6 \times 6} & 0_{6 \times 6} \end{bmatrix} \quad W = \begin{bmatrix} 0_{6 \times 6} & I_{6 \times 6} \end{bmatrix} \quad (20)$$

The state vector x includes the inertial position p , orientation η , and their respective derivatives $\dot{p}, \dot{\eta}$. Only the pose (position and orientation) is taken as the system's output, while \dot{p} and $\dot{\eta}$ are estimated through the observer. According to (11), (12), the smallest integer satisfying the above condition is $L = 2$, with the invertibility and observability matrices assuming the form

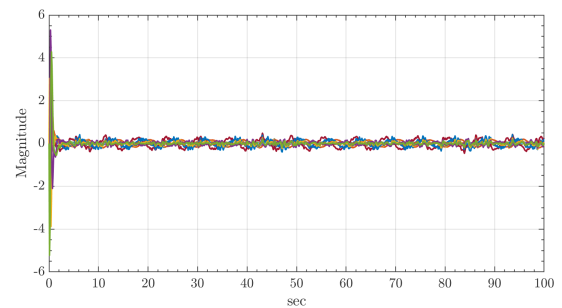
$$J^2 = \begin{bmatrix} 0 & 0 & 0 \\ CW & 0 & 0 \\ CAW & CW & 0 \end{bmatrix}, \quad O^2 = \begin{bmatrix} C \\ CA \\ CA^2 \end{bmatrix} \quad (21)$$

for which it holds, based on (19), (20), $rank(J) = 6$ and $rank(O) = 12$, thus satisfying the conditions of solvability.

The state estimation error for the EKF and the UIO is given in Figure 9. The UIO tracks the states even in



(a) EKF state estimation error



(b) UIO state estimation error

Fig. 9: UIO and EKF comparison

the presence of external disturbances and more effectively than the EKF. Even in the presence of sensor bias, the UIO demonstrates robustness to the noise maintaining an accurate estimate of the states and a corresponding smaller error magnitude, also not requiring any information about the unknown inputs, here in the form of external disturbance. The computed Root Mean Square Error (RMSE) for both the EKF and the UIO is given in Table VI.

As a second validation step, based on the results gained

TABLE VI: UIO and EKF RMSE, Simulink Comparison

| RMSE | Position | Orientation | Linear vel | Ang vel |
|------|----------|-------------|------------|---------|
| UIO | 0.18 | 0.09 | 0.25 | 0.47 |
| EKF | 0.31 | 0.30 | 2.87 | 0.48 |

from the analysis in Matlab/Simulink, the UIO is tested in the simulator architecture in order to both test and assess the algorithm's robustness to external disturbances and measurement uncertainties, and to obtain a software-in-the-loop validation of the proposed system implementa-

tion. The simulation results carried out in the simulator for the analyzed mission are presented in Table VII and Figure 10. The wind is applied along the horizontal direction (\bar{v}_w) with a maximum intensity of 4m/sec, and vertically up to 1 m/sec ($\bar{v}_{w,z}$). As shown, the UIO is able to estimate the unknown states of the system (velocities), having the pose as input. The estimated states closely track the original states without significant drift or deviation from the reference, with the most significant impact during the landing phase. The overall accuracy of the proposed method is validated by the RMSE measurements.

TABLE VII: UIO RMSE, *Simulator*

| UIO estimate | Position | Orientation | Linear vel | Ang vel |
|--------------|----------|-------------|------------|---------|
| RMSE | 0.22 | 0.72 | 0.23 | 0.11 |

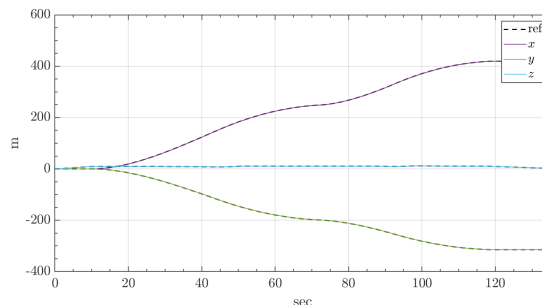
2. Controller Comparison

Table VIII gives the comparison between the RMSE of the attitude with respect to desired attitude trajectory along with the different control approaches implemented. Two different simulated experiments are performed in the simulator architecture: in the first, only the sensor noises are taken into account without other external disturbances, testing smooth flight conditions. In the second one, both wind along horizontal (\bar{v}_w) and vertical ($\bar{v}_{w,z}$) directions and sensor bias are considered.

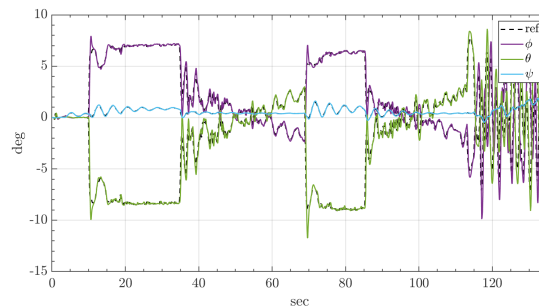
TABLE VIII: MHex controllers RMSE, *Simulator*

| RMSE [deg] | A-PID | PID FL | BC |
|------------|-------|--------|------|
| No Wind | 4.23 | 1.82 | 3.78 |
| Wind | 9.36 | 1.37 | 3.96 |

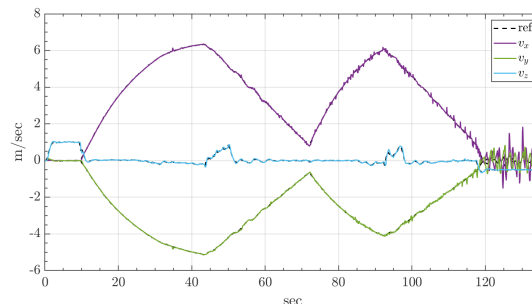
As shown, the model-based control approaches are able to achieve smaller RMSE compared to the *A-PID* controller. The propeller angular velocity during cruise remains in the range of $M = 0.55$ to 0.8 at tip, corresponding to 1910 to 2780 rpm (200 rad/sec to 291 rad/sec respectively, with max peaks of 315 rad/sec (3008 rpm, $M = 0.86$)). Considering the flight speed as ground speed, the limit of 8 m/s guarantees that the linear velocity at the propeller tip is less than $M = 0.89$. The propeller angular velocity has an average of 260 rad/sec (2483 rpm, $M = 0.71$), and a median of 265 rad/sec (2531 rpm, $M = 0.73$), resulting close to the blade optimum operating point of $M = 0.75$, based on the data available in [8], as shown in plots in IX. The resulting control gains for each controller show the ability of the tuning process to achieve the best performances while avoiding saturation of the control action, while the propeller rates, displayed in Figure 11 remain bounded and stable for all controller strategies. Finally, given the overall better performance, even during wind simulations, the model-based approaches are preferable for mapping and navigation tasks.



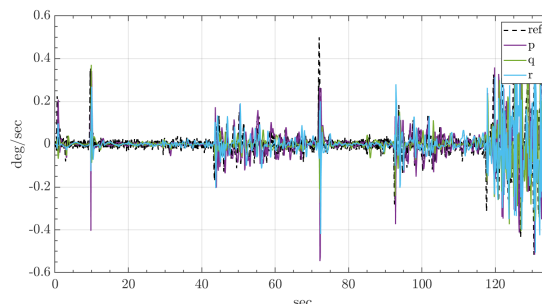
(a) Position



(b) Orientation



(c) Linear velocity



(d) Angular velocity

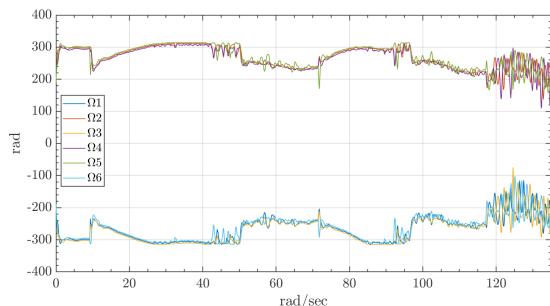
Fig. 10: UIO state estimation

3. Mapping Experiment

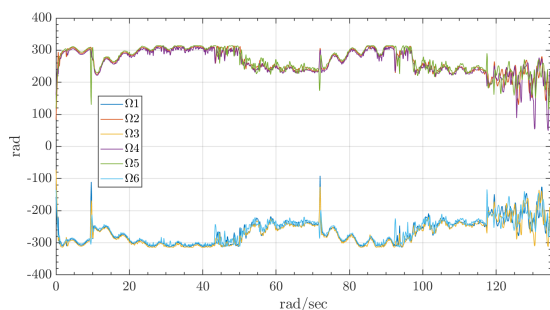
Figure 10 shows the mapping process in the explored site based on the point cloud feature extraction. As reported in Section 2, when performing SLAM both the edge and planar features are extracted from the same lidar scan, and the corresponding feature subset is first

TABLE IX: Controller Gains

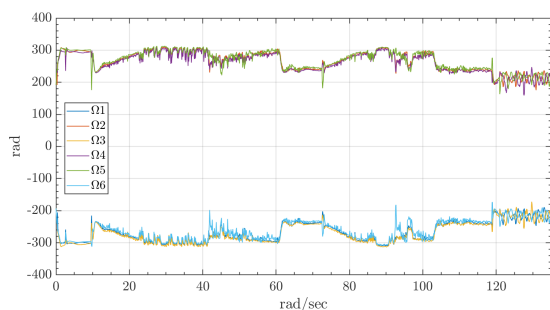
| Gains <i>PID</i> | $K_{p,prefilter}$ | K_p | K_i | K_d |
|------------------|-----------------------------|----------------------------|-----------------------------|-------------------------|
| <i>PID-AP</i> | $4.5 \times I_{3 \times 3}$ | diag(0.135, 0.135, 0.180) | diag(0.135, 0.135, 0.018) | diag(0.0036, 0.0036, 0) |
| <i>PID-FL</i> | $9 \times I_{3 \times 3}$ | diag(1.25, 1.25, 0.50) | $0.1 \times I_{3 \times 3}$ | diag(0.01, 0.01, 0) |
| Gains <i>BC</i> | K_r | K_i | Λ | -- |
| <i>BC</i> | $1 \times I_{3 \times 3}$ | $30 \times I_{3 \times 3}$ | $1 \times I_{3 \times 3}$ | -- |



(a) *A-PID*



(b) *PID-FL*



(c) *BC*

Fig. 11: MHex propeller angular velocity, simulated experiment including wind

optimized through point cloud segmentation and then processed by the mapping module. This procedure allows for a reduction of the number of points stored in the map, also filtering out unstable features based on the c_{th} threshold. The SLAM algorithm is able to track morphological features of the crater while performing real-time pose estimation. The VLP-16 provides precise and direct depth measurements in the environment, resulting in accurate 3D point cloud data even in a wide and feature-poor scenario such as Martian terrain. Moreover, since the entire mapping process results optimized in terms of ground point cloud segmentation, the lidar-mapping accuracy is improved, reducing the computational complexity when compared to the vision-based counterpart. Last but not least, the lidar FoV results in a wide range of collecting data thus particularly valuable when a thorough comprehension of the environment is essential during long-range exploration.

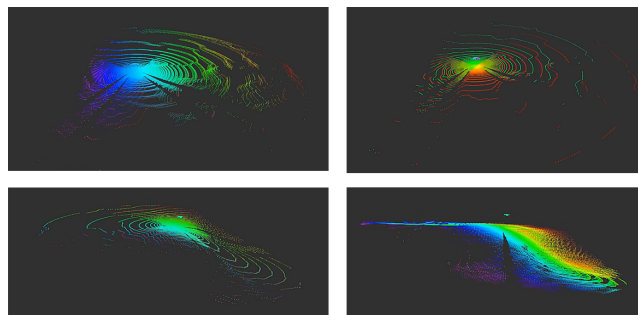


Fig. 12: *MHex* mapping framework: The *MHex* approaches the crater and performs the point cloud map. Edge and planar features are progressively extracted, and selected subsets of points are then stored in the final map

V. Conclusions

This article presented a system analysis for a future Martian hexacopter. After deriving a conceptual architecture and sizing of the MHex prototype, autonomous navigation based on a realistic mission scenario along with SLAM and 3D mapping showed the capability of accurate mapping and stratigraphic investigation of the surrounding environment, addressing the numerous challenges of Martian flight together with the comparison of different control strategies. To validate the entire GNC analysis, a simulator architecture based on free and open-source software (ROS, Gazebo, and Ardupilot)

was proposed, and the simulated experiments considering both state estimation and model-based control were performed with promising results. Realistic SITL features included, along with Martian environmental conditions, sensor noises, aerodynamic and wind effects, VLP-16 Lidar rotating dynamics, GPS-denied position estimates, and conservative sampling rates. Firstly, an enhanced UIO was presented and compared to the well-known EKF for filtering sensor output, showing robustness against disturbances and sensor bias, guaranteeing accurate estimates of the unknown states and overcoming the limitations of different classes of filters more sensitive to external disturbances. Secondly, a comparison between model-based control strategies (*PID-FL* and *BC*) and the stock Ardupilot attitude PID controller (*A-PID*) showed the advantage of considering the MHex nonlinear dynamics for achieving a more precise control and compensating for the tight flight envelope and environmental conditions characterizing the flying on Mars. Finally, even if experimental verification of both rotor structural design and aerodynamic performance is required to validate the entire MHex architecture, the presented examination of the hexacopter gave consistency and substantial capability for autonomous operation on Mars in the context of future exploration. Moreover, the Ardupilot integration (or any other flight controller unit) in the simulator pipeline will allow for reducing the effort required to transition from SITL to hardware in the loop (HITL). The authors intend to share the code and documentation to enable other researchers to test their applications on the presented simulator architecture.

REFERENCES

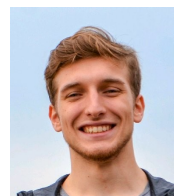
- [1] J. Simon *et al.*
Samples collected from the floor of jezero crater with the mars 2020 perseverance rover
Journal of Geophysical Research: Planets, vol. 128, no. 6, p. e2022JE007474, 2023.
- [2] J. Balaram, M. Aung, and M. P. Golombek
The ingenuity helicopter on the perseverance rover
Space Science Reviews, vol. 217, no. 4, p. 56, 2021.
- [3] T. Tzanetos *et al.*
Ingenuity mars helicopter: From technology demonstration to extraterrestrial scout
In *2022 IEEE Aerospace Conference (AERO)*. IEEE, 2022, pp. 01–19.
- [4] G. Kminek, M. A. Meyer, D. W. Beaty, B. L. Carrier, T. Haltigin, and L. E. Hays
Mars sample return (msr): planning for returned sample science
Astrobiology, vol. 22, no. S1, pp. S–1, 2022.
- [5] F. Mier-Hicks *et al.*
Sample recovery helicopter
In *2023 IEEE Aerospace Conference*. IEEE, 2023, pp. 1–11.
- [6] L. Sopegno, K. P. Valavanis, M. J. Rutherford, and L. Casalino
Mars sample return mission: mars ascent vehicle propulsion design
In *2020 IEEE Aerospace Conference*. IEEE, 2020, pp. 1–9.
- [7] A. Elsaesser *et al.*
Future space experiment platforms for astrobiology and astrochemistry research
npj Microgravity, vol. 9, no. 1, p. 43, 2023.
- [8] W. Johnson *et al.*
Mars science helicopter conceptual design
Tech. Rep., 2020.
- [9] J. Balaram, I. Daubar, J. Bapst, and T. Tzanetos
Helicopters on mars: Compelling science of extreme terrains enabled by an aerial platform
In *Ninth International Conference on Mars*, vol. 2089, 2019, p. 6277.
- [10] T. Tzanetos *et al.*
Future of mars rotorcraft-mars science helicopter
In *2022 IEEE Aerospace Conference (AERO)*. IEEE, 2022, pp. 1–16.
- [11] H. F. Grip *et al.*
Guidance and control for a mars helicopter
In *2018 AIAA Guidance, Navigation, and Control Conference*, 2018, p. 1849.
- [12] S. Pedone, M. Trumić, K. Jovanović, and A. Fagiolini
Robust and decoupled position and stiffness control for electrically-driven articulated soft robots
IEEE Robotics and Automation Letters, vol. 7, no. 4, pp. 9059–9066, 2022.
- [13] H. Lu, H. Shen, B. Tian, X. Zhang, Z. Yang, and Q. Zong
Flight in gps-denied environment: Autonomous navigation system for micro-aerial vehicle
Aerospace Science and Technology, vol. 124, p. 107521, 2022.
- [14] J. Zhang and S. Singh
Loam: Lidar odometry and mapping in real-time. In *Robotics: Science and systems*, vol. 2, no. 9. Berkeley, CA, 2014, pp. 1–9.
- [15] T. Shan and B. Englot
Lego-loam: Lightweight and ground-optimized lidar odometry and mapping on variable terrain
In *2018 IEEE/RSJ International Conference on Intelligent Robots and Systems (IROS)*. IEEE, 2018, pp. 4758–4765.
- [16] T. H. Chan, H. Hesse, and S. G. Ho
Lidar-based 3d slam for indoor mapping
In *2021 7th International Conference on Control, Automation and Robotics (ICCAR)*. IEEE, 2021, pp. 285–289.
- [17] X. Xu *et al.*
A review of multi-sensor fusion slam systems based on 3d lidar
Remote Sensing, vol. 14, no. 12, p. 2835, 2022.
- [18] R. Milijaj, L. Markovic, A. Ivanovic, F. Petric, and S. Bogdan
A comparison of lidar-based slam systems for control of unmanned aerial vehicles
In *2021 International Conference on Unmanned Aircraft Systems (ICUAS)*. IEEE, 2021, pp. 1148–1154.
- [19] A. Patel, A. Banerjee, B. Lindqvist, C. Kanellakis, and G. Nikolakopoulos
Design and model predictive control of a mars coaxial quadrotor
In *2022 IEEE Aerospace Conference (AERO)*. IEEE, 2022, pp. 1–11.
- [20] S. Dutta, C. D. Karlgaard, D. Kass, M. Mischna, and G. G. Villar III
Postflight analysis of atmospheric properties from mars 2020 entry, descent, and landing
Journal of Spacecraft and Rockets, vol. 60, no. 3, pp. 1022–1033, 2023.
- [21] Ardupilot
Copter attitude control. [Online]. Available: <https://ardupilot.org/dev/docs/apmcopter-programming-attitude-control-2.html>
- [22] C. Vleugels, B. Foing, and O. Swida
A comparison of perseverance rover and hirise data: siteinterpretations in jezero crater
Copernicus Meetings, Tech. Rep., 2023.
- [23] V. Z. Sun and K. M. Stack
Geologic map of jezero crater and the nili planum region, mars
Scientific Investigations Map, 2020. [Online]. Available: <https://api.semanticscholar.org/CorpusID:229665623>
- [24] V. Zappek, M. Rinker, L. Daxer, and M. Hajek
Evaluation of aerial vehicle configurations for high-range mars missions
CEAS Space Journal, pp. 1–15, 2023.

- [25] L. Sopegno, P. Livreri, K. Valavanis *et al.* Using uavs for future mission on mars In *Proceedings of the International Astronautical Congress, IAC*, vol. 2022. International Astronautical Federation, IAF, 2022.
- [26] M. Radotich A study of past, present, and future mars rotorcraft 2021. [Online]. Available: <https://api.semanticscholar.org/CorpusID:234777444>
- [27] P. G. Jayasekara, G. Ishigami, and T. Kubota Testing and validation of autonomous navigation for a planetary exploration rover using opensource simulation tools In *International Symposium on Artificial Intelligence, Robotics and Automation in Space, ISAIRAS*, 2012.
- [28] J. I. Giribet, R. S. Sanchez-Pena, and A. S. Ghersin Analysis and design of a tilted rotor hexacopter for fault tolerance *IEEE Transactions on Aerospace and Electronic Systems*, vol. 52, no. 4, pp. 1555–1567, 2016.
- [29] Hovermap (2023) Hovermap 3d lidar. Accessed: September 2023. [Online]. Available: <https://im-mining.com/2019/02/02/emesent-hovermap-first-autonomous-lidar-mapping-payload-mining-drones/>
- [30] D. R. Cremons The future of lidar in planetary science *Frontiers in Remote Sensing*, vol. 3, p. 1042460, 2022.
- [31] P. Lee, E. Kommedal, A. Horchler, E. Amoroso, K. Snyder, and A. Birgisson Lofthellir lava tube ice cave, iceland: Subsurface micro-glaciers, rockfalls, drone lidar 3d-mapping, and implications for the exploration of potential ice-rich lava tubes on the moon and mars In *50th Annual Lunar and Planetary Science Conference*, no. 2132, 2019, p. 3118.
- [32] F. Amzajerjian, D. Pierrottet, G. D. Hines, L. Petway, B. Barnes, and J. M. Carson Development of navigation doppler lidar for future landing missions In *AIAA SPACE 2016*, 2016, p. 5590.
- [33] I. Velodyne Lidar Velodyne vlp-16 lidar 2023, datasheet.
- [34] IntelRealSense t256 tracking camera 20XX, datasheet camera.
- [35] Garmin (2023) Altimeter garmin v3 lite. Accessed: September 2023. [Online]. Available: <https://www.garmin.com/en-US/blog/general/garmin-on-mars/>
- [36] P. Li, D. Liu, X. Xia, and S. Baldi Embedding adaptive features in the ardupilot control architecture for unmanned aerial vehicles In *2022 IEEE 61st Conference on Decision and Control (CDC)*. IEEE, 2022, pp. 3773–3780.
- [37] P. Li, D. Liu, and S. Baldi Adaptive integral sliding mode control in the presence of state-dependent uncertainty *IEEE/ASME Transactions on Mechatronics*, vol. 27, no. 5, pp. 3885–3895, 2022.
- [38] S. Baldi, D. Sun, X. Xia, G. Zhou, and D. Liu Ardupilot-based adaptive autopilot: Architecture and software-in-the-loop experiments *IEEE Transactions on Aerospace and Electronic Systems*, vol. 58, no. 5, pp. 4473–4485, 2022.
- [39] S. Martini, S. Sönmez, A. Rizzo, M. Stefanovic, M. J. Rutherford, and K. P. Valavanis Euler-lagrange modeling and control of quadrotor uav with aerodynamic compensation In *2022 International Conference on Unmanned Aircraft Systems (ICUAS)*. IEEE, 2022, pp. 369–377.
- [40] Ardupilot (2023) Ardupilot copter. Accessed: September 2023. [Online]. Available: <https://ardupilot.org/copter/docs/common-autopilots.html>
- [41] S. I. Azid, K. Kumar, M. Cirrincione, and A. Fagiolini Robust motion control of nonlinear quadrotor model with wind disturbance observer *IEEE Access*, vol. 9, pp. 149 164–149 175, 2021.
- [42] S. Pedone and A. Fagiolini Racecar longitudinal control in unknown and highly-varying driving conditions *IEEE Trans. on Vehicular Technology*, vol. 69, no. 11, pp. 12 521–12 535, 2020.
- [43] S. Sundaram and C. N. Hadjicostis Delayed observers for linear systems with unknown inputs *IEEE Trans. on Automatic Control*, vol. 52, no. 2, pp. 334–339, 2007.
- [44] B. Siciliano, L. Sciavicco, L. Villani, and G. Oriolo *Robotics: modelling, planning and control*. Springer Science & Business Media, 2010.
- [45] S. Martini, M. Stefanovic, A. Rizzo, M. J. Rutherford, P. Livreri, and K. P. Valavanis A benchmark framework for testing, evaluation, and comparison of quadrotor linear and nonlinear controllers In *2023 International Conference on Unmanned Aircraft Systems (ICUAS)*. IEEE, 2023, pp. 471–478.
- [46] A. Das, F. Lewis, and K. Subbarao Backstepping approach for controlling a quadrotor using lagrange form dynamics *Journal of Intelligent and Robotic Systems*, vol. 56, no. 1, pp. 127–151, 2009.



Laura Sopegno is a PhD student in the Electrical Engineering Department at the University of Palermo and the Electrical and Computer Engineering Department at the University of Denver. She received her Master's Degree in Aerospace Engineering, Space and Propulsion Systems, at the Polytechnic of Turin in 2019. She worked on the Mars Sample Return mission at Thales Alenia Space Company, Italy, from 2020 to 2021. Dr. Sopegno research inter-

ests span from propulsion systems for space applications to the autonomous guidance, navigation and control architectures of Unmanned Aerial Vehicles (UAVs) with a principal focus on future Mars and Moon exploration.



Simone Martini is a PhD candidate in the Electrical and Computer Engineering department at the University of Denver, working under the supervision of Dr. Kimon P. Valavanis at University of Denver Unmanned Systems Research Institute (DU²SRI) and Dr. Alessandro Rizzo at Politecnico di Torino. From August 2022 to June 2023 he also worked in collaboration with University of Palermo under supervision of Dr. Livreri supported by Progetto

“SEAVIEW”, Azione 1.1.5, PO FESR 2014/2020. He obtained his B.S. in Aerospace Engineering and M.S. in Mechatronics Engineering from Politecnico di Torino. His research interest revolve around nonlinear modeling and control of UAV.



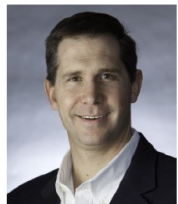
Salvatore Pedone is a Researcher and Lecturer of Automatic Control at the University of Palermo, Italy. He received his M.S. degree in Aerospace Engineering in 2018 and his Ph.D. degree in Information and Communication Technologies in 2023 from the University of Palermo. His research interests are in the design and development of control and estimation methods for complex nonlinear systems as self-driving vehicles, unmanned aerial vehicles and

soft articulated robots.



Adriano Fagiolini is an Associate Professor at the University of Palermo, Italy. He received an M.S. degree in Computer Science Engineering in 2004 and a Ph.D. degree in Robotics and Automation in 2009 from the University of Pisa. He has been a Visiting Researcher at the Department of Energy, IUT Longwy, Université de Lorraine (France) in 2019, and the Department of Mechanical Engineering, University of California at Riverside, in 2015 and 2017. He

enrolled in the Summer Student Programme at the European Center for Nuclear Research (CERN), Geneva, in 2002, and in the International Curriculum Option of Doctoral studies in Hybrid control for complex, distributed, and heterogeneous embedded systems in 2007. In 2008, he led the team of the University of Pisa during the first European Space Agency's Lunar Robotics Challenge, which resulted in a second-place prize for the team. He was one of the recipients of the IEEE ICRA's Best Manipulation Paper Award in 2005. He is an Associate Editor of the IEEE Robotics and Automation Letters (RA-L) since 2018, of the newly launched Robotics Reports Journal by Mary Ann Liebert since 2023, and of the IEEE International Conference on Robotics and Automation (ICRA) and IEEE/RSJ International Conference on Intelligent Robots (IROS) since 2017. He is a member of the IFAC Technical Committee on Control and Education since 2020.



Matthew J. Rutherford is an Associate Professor in the Department of Computer Science with a joint appointment in the Department of Electrical and Computer Engineering at the University of Denver. He is also Deputy Director of the DU Unmanned Systems Research Institute (DU²SRI). His research portfolio includes: the development of advanced controls and communication mechanisms for autonomous aerial and ground robots; applica-

tions of real-time computer vision to robotics problems using GPU-based parallel processing; testing and dynamic evaluation of embedded, real-time systems; development of complex mechatronic systems (mechanical, electrical, and software); the development of software techniques to reduce the amount of energy being consumed by hardware; development of a high-precision propulsion system for underwater robots.



Margareta Stefanovic (S'03–M'05) received the Dipl.-Ing. degree from the University of Nis, Yugoslavia, in 1996, and the M.Sc. and Ph.D. degrees in electrical engineering from the University of Southern California, Los Angeles, in 2002 and 2005, respectively. She joined the University of Wyoming, Laramie, in 2005 as an Assistant Professor in the Electrical and Computer Engineering Department. Her current research interests include switching adap-

tive control of uncertain systems and coordinated control and decision

making in hyper-spectral imaging nano-satellite networks for Space Situational Awareness.



Alessandro Rizzo received the Laurea degree (summa cum laude) in computer engineering and the Ph.D. degree in automation and electronics engineering from the University of Catania, Italy, in 1996 and 2000, respectively. In 1998, he worked as a EURATOM Research Fellow with JET Joint Undertaking, Abingdon, U.K., researching on sensor validation and fault diagnosis for nuclear fusion experiments. In 2000 and 2001, he has worked as a Research

Consultant at ST Microelectronics, Catania Site, Italy, and as an Industry Professor of robotics with the University of Messina, Italy. From 2002 to 2015, he was a tenured Assistant Professor with the Politecnico di Bari, Italy. Since 2012, he has been a Visiting Professor with the New York University Tandon School of Engineering, Brooklyn, NY, USA. In November 2015, he joined Politecnico di Torino, where he is an Associate Professor in the Department of Electronics and Telecommunications and established the Complex Systems Laboratory. Dr. Rizzo is engaged in conducting and supervising research on cooperative robotics, complex networks and systems, modeling and control of nonlinear systems. He is the author of two books, two international patents, and more than 200 papers on international journals and conference proceedings. He was the recipient of the Award for the Best Application Paper at the IFAC world triennial conference in 2002 and of the Award for the Most Read Papers in Mathematics and Computers in Simulation (Elsevier) in 2009. He has also been a Distinguished Lecturer of the IEEE Nuclear and Plasma Science Society and one of the recipients of the 2019 and 2021 Amazon Research Awards in robotics.



Patrizia Livreri (SM, IEEE) PhD, is a Professor of Electronics with the Department of Engineering, at the University of Palermo. She received her "Laurea degree" (Hons.) in Electronics Engineering in 1986 and her Ph.D. in ICT in 1992, both from the University of Palermo, Italy. From 1993 to 1994, she was a researcher at CNR, Rome, Italy. Since 1994, she was an assistant professor at the University of Palermo, Italy. Since 2017, she has been

the Director of the Power Electronics Laboratory. Since 2020, she has been the Director of the Microwave Power Laboratory. In 2020, she also joined the National Laboratory for Radar and Surveillance Systems in Pisa, Italy. Since 2021, she has been a Visiting Professor at the San Diego State University, CA, USA. Prof. Livreri research interests are in microwave power amplifiers, high power microwave source, antennas, radar, and UAV. She has authored or co-authored more than 250 published papers and served as an invited speaker and Keynote speaker at international conferences. She has been selected to serve NATO Science and Technology Organization (STO) as an Invited Speaker for Quantum Technology. She is the principal investigator of the "Microwave Quantum Radar" project, funded by the Ministry of Defense, the supervisor of many funded projects. She was the recipient of the Award for Best Paper at the IEEE ICRERA Conference in 2017. Since 2023, she has been serving as an IEEE Access Associate Editor.



Kimon P. Valavanis (SM, IEEE) PhD, is John Evans Professor, Department of ECE, D. F. Ritchie School of Engineering and Computer Science, University of Denver. He is Guest Professor in the Faculty of Electrical Engineering and Computing, University of Zagreb, Croatia. He also held Visiting Appointments at Politecnico di Torino, Dipartimento di Ingegneria Meccanica e Aerospaziale, DIMEAS, and he was Professeur Invité, Université de Lorraine

- Polytech Nancy, in France. His research interests span Unmanned Systems, Distributed Intelligence Systems, Robotics and Automation. He has published more than 450 book chapters, technical journal, and transaction, referred conference, and invited papers. He has authored/co-authored/edited 19 books. He has graduated 40 PhD students and more than 100 M.Sc. students. Dr. Valavanis served as Editor-in-Chief of the Robotics and Automation Magazine from 1996-2005, and since 2006, of the Journal of Intelligent and Robotic Systems, Springer. He also serves as co-chair of the Aerial Robotics and Unmanned Aerial Vehicles Technical Committee since 2008. He founded the International Conference on Unmanned Aircraft Systems, which he runs annually. Dr. Valavanis was a Distinguished Speaker in the IEEE Robotics and Automation Society, a Senior Member of IEEE, a Fellow of the American Association for the Advancement of Science, a Fellow of the U.K. Institute of Measurement and Control, and a Technical Expert of the NATO Science and Technology Organization (STO). He was also selected to serve as NATO Technical Evaluator for the AVT-353 Workshop on 'Artificial Intelligence in the Cockpit for UAVs' that will take place in Torino, Italy, in April 2022. In August of 2021, he was also appointed to the NATO STO Technical Team of SAS-ET-EX on "Integration of Unmanned Systems into Operational Units" for the duration of the Program of Work. He is also a Fulbright Scholar (Senior Lecturing & Research Award).